

# ASCA Observations of OAO 1657–415 and its Dust-Scattered X-Ray Halo

Michael. D. Audley<sup>1,2\*</sup>, Fumiaki Nagase<sup>3</sup>, Kazuhisa Mitsuda<sup>3</sup>,  
 Lorella Angelini<sup>4,5</sup>, & Richard. L. Kelley<sup>4</sup>

<sup>1</sup>UK Astronomy Technology Centre, Royal Observatory, Blackford Hill, Edinburgh EH9 3HJ

<sup>2</sup>Present address: Cavendish Laboratory, University of Cambridge, Madingley Road, Cambridge CB3 0HE

<sup>3</sup>Institute of Space and Astronautical Science, 3-1-1 Yoshinodai, Sagamihara, Kanagawa 229-8510, Japan

<sup>4</sup>Code 662, NASA / Goddard Space Flight Center, Greenbelt, MD 20771, USA

<sup>5</sup>Department of Physics and Astronomy, Johns Hopkins University, Baltimore, MD, 21218, USA

27 August 2018

## ABSTRACT

We report on two ASCA observations of the high-mass X-ray binary pulsar OAO 1657–415. A short observation near mid-eclipse caught the source in a low-intensity state, with a weak continuum and iron emission dominated by the 6.4-keV fluorescent line. A later, longer observation found the source in a high-intensity state and covered the uneclipsed through mid-eclipse phases. In the high-intensity state, the non-eclipse spectrum has an absorbed continuum component due to scattering by material near the pulsar and 80 per cent of the fluorescent iron emission comes from less than 19 lt-sec away from the pulsar. We find a dust-scattered X-ray halo whose intensity decays through the eclipse. We use this halo to estimate the distance to the source as  $7.1 \pm 1.3$  kpc.

**Key words:** X-rays: binaries – X-rays: individual: OAO 1657–415 – X-rays: ISM – dust, extinction

## 1 INTRODUCTION

OAO 1657–415 is one of the most poorly studied eclipsing high mass X-ray binary systems, and yet is potentially one of the most interesting. The reason this system is not so well known is because it took 15 years for its nature as a high mass X-ray binary to be revealed. OAO 1657–415 was discovered with the *Copernicus* satellite (Polidan et al. 1978). A subsequent observation with *HEAO-1* revealed a pulse period of 38 s (White & Pravdo 1979). The 3–30 keV *Ginga* spectrum (Kamata et al. 1990) is a typical X-ray pulsar spectrum with a power law ( $\alpha \sim 0.6$ ), a high energy cutoff ( $E_c \sim 5$  keV and  $E_f \sim 17$  keV) and an iron line at 6.6 keV (equivalent width  $\sim 240$  eV).

For many years it was unclear if OAO 1657–415 was a low-mass or a high-mass system. The mystery was cleared up when the *CGRO* BATSE discovered a  $\sim 10.4$ -d binary orbit based on long term monitoring of the pulse period in the 20–40 keV band (Chakrabarty et al. 1993). A  $\sim 1.7$  day eclipse of the X-ray source by its companion was also seen. This conclusively showed OAO 1657–415 to be a classic eclipsing massive X-ray binary system, probably similar to Vela X-1, making it the seventh eclipsing X-ray pulsar

system to be found. Chakrabarty et al. (1993) used the orbital parameters to infer that the companion is a supergiant of spectral class B0–B6. From the observed value of the spin period and its derivative during the spin-up interval they deduced an X-ray luminosity of  $\gtrsim 1.6 \times 10^{37}$  ergs s<sup>−1</sup>, and thus a distance of  $\gtrsim 11$  kpc. A more precise X-ray location obtained with Chandra allowed Chakrabarty et al. (2002) to make an infrared identification of the companion. The infrared properties of the companion are consistent with a highly-reddened B supergiant at a distance of  $6.4 \pm 1.5$  kpc, implying an X-ray luminosity of  $3 \times 10^{36}$  ergs<sup>−1</sup>.

OAO 1657–415’s position on the Corbet diagram (Corbet 1986) suggests that it may not be a typical system. The pulse periods of high-mass X-ray binaries (HMXRB) are distributed between 0.069 and 835 s, with no evidence for a clustering at any particular period. For the Be star systems there is a strong correlation between orbital period,  $P_o$ , and spin period,  $P_s$ . The supergiant systems have no strong dependence of orbital period on spin period. OAO 1657–415’s 38 sec pulsar with its 10.4-d orbital period lies between the Be and supergiant systems on the Corbet diagram. The period measurements from *RXTE*, BATSE, and previous observations give a steady spin-up timescale of 125 yr (Baykal 1997) with short-term fluctuations (Baykal 2000). This system may be in a short-lived phase where it is changing from

\* E-mail: audley@mrao.cam.ac.uk

a wind-accreting system like Vela X-1 to a disk-accreting system like Cen X-3. Thus, OAO 1657–415 provides an opportunity to test wind and/or disk accretion theory on a system which is in a transition between the two states.

## 2 THE OBSERVATIONS

OAO 1657–415 was observed near the middle of its eclipse on 1994 March 24, yielding 22 ks of data. This observation covered orbital phases  $-0.001$ – $0.074$ . It was observed later (near 1997 September 17) through its eclipse ingress for 200 ks. This observation, covering orbital phase  $-0.210$ – $0.011$ , yielded 67 ks of SIS data. The orbital phases in this paper are calculated using the ephemeris of Bildsten et al. (1997). For both of the observations the SIS was operated in one-CCD bright mode and the GIS in PH mode. The eclipse spectra were significantly different between the two observations. We discuss these differences in Section 4.1.

## 3 RESULTS

### 3.1 Timing analysis

#### 3.1.1 The Light Curve

Energy-resolved SIS lightcurves and hardness ratios for the second observation are shown in Fig. 1. The eclipse transition is extended, with the high-energy band becoming fully obscured around orbital phase  $-0.09$ . The flux in the low energy bands decays gradually in the eclipse, suggesting the presence of a persistent soft excess.

#### 3.1.2 The pulse profile

We derived a barycentric pulse period of  $37.39 \pm 0.01$  s from the non-eclipse part of the 1997 observation. The pulse profile from the 1997 observation is qualitatively similar to the 1–20 keV pulse profile observed by Kamata et al. (1990) with the GINGA LAC. Most of the power is in the first harmonic. The pulsed fraction also increases with energy, as would be expected for a source with such a high absorbing column density ( $\sim 5 \times 10^{22}$  cm $^{-2}$ ). The dip which occurs after the main peak (labeled ‘A’ in Fig. 2) seems to be sharper in the present data than in the GINGA data. When the 1–10 keV GIS2 and GIS3 data from the first 30 ks of the observation are folded into 256 pulse-phase bins, dip A has a Gaussian width ( $\sigma$ ) in pulse phase of  $0.0256 \pm 0.0054$  at 90 per cent confidence. This corresponds to a duration of  $0.96 \pm 0.20$  s. The main dip corresponding to the pulse minimum (labeled ‘B’ in Fig. 2) has a width of  $0.097 \pm 0.019$  in pulse phase, or a duration of  $3.6 \pm 0.7$  s. Sharp dips in the pulse profile have also been seen in Vela X-1 (e.g. Choi et al. 1996), LMC X-4 (e.g. Levine et al. 1991), and GX 1+4 (e.g. Dotani et al. 1989). The pulsed fraction in the pulse profile of OAO 1657–415 increases with energy, suggesting that the pulsating component of the continuum is subjected to more absorption than the non-pulsating component.

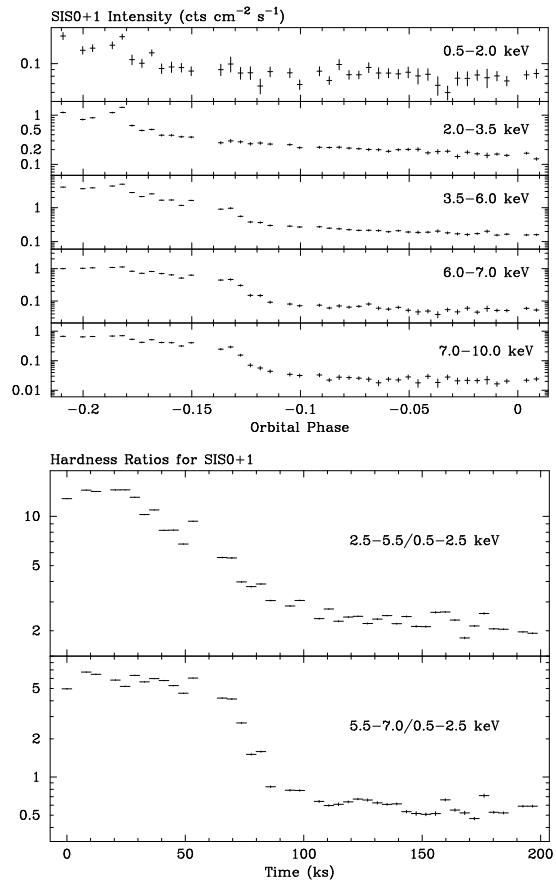


**Figure 1.** Top: Energy-resolved SIS lightcurves observed during the second ASCA observation. The slow decay of the intensity in the low-energy bands through the eclipse is due to the decaying dust halo. Bottom: SIS hardness ratios. Note that the lightcurves are plotted against orbital phase, while the hardness ratios are plotted against time from the start of the observation. Both are plotted over the same range to allow direct comparison.

### 3.2 Spectroscopy

The standard screening criteria were applied to the data and GIS spectra were extracted from circular regions with radii of 6 arcmin. Because this source is near the Galactic plane, where contamination from the Galactic ridge can be significant (e.g. Koyama et al. 1989), the standard background spectra accumulated from blank-sky observations could not be used. Thus, we extracted background spectra from source-free regions of the detectors. To account for the azimuthal dependence of the XRT spatial response, background spectra for the GIS data were extracted from circular regions whose centres were obtained by reflecting the source coordinates through the optical axis. To avoid oversubtraction of the source, only eclipse data were used for the background, and the part of the background region less than 8 arcmin from the source was excluded. SIS Bright mode spectra were extracted from 4-arcmin circles around the source. Background spectra were extracted from the part of the chip more than 6 arcmin away from the source, using only eclipse data.

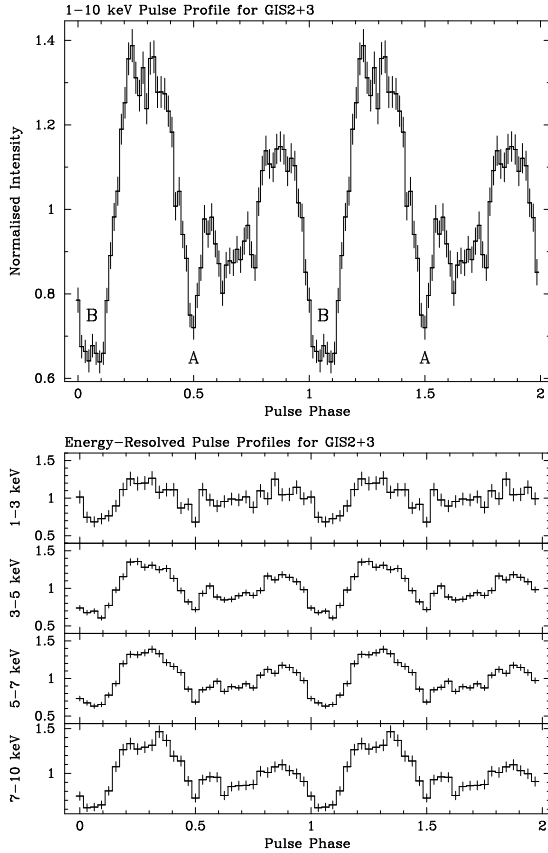


**Figure 2.** Top: GIS 2+3 energy-averaged pulse profile. The dips in the profile labeled ‘A’ and ‘B’ are discussed in the text. Bottom: GIS 2+3 energy-resolved pulse profiles.

### 3.2.1 The non-eclipse spectrum

Referring to Fig. 1, the source is essentially uneclipsed for the first 30 ks of the observation, or orbital phases  $\phi = -0.210 - -0.177$ . We extracted spectra for this interval, added the two SIS and GIS detectors, and fitted a model of the form

$$I(E) = e^{-\sigma EN_{Hl}} (I_d E^{-\alpha} + e^{-\sigma EN_{Hl}} I_s E^{-\alpha} + I_h E^{-(\alpha+2)}) + I_{fl} e^{-(E-E_{fl})^2/2\sigma_{fl}^2} + I_{rc} e^{-(E-E_{rc})^2/2\sigma_{rc}^2} \quad (1)$$

simultaneously to the SIS and GIS data. The continuum is represented by a power law plus a heavily absorbed power law with the same photon index,  $\alpha$ . We interpret these as representing direct and scattered emission from the pulsar. As Thomson scattering is a colourless process the power laws have the same index. To model the dust-scattered halo we included a power law with a photon index  $\alpha + 2$  and the same absorption column density as the direct emission power law. We included two Gaussian emission lines, due to fluorescence of cold iron and recombination of H- and He-like iron, labelled with the subscripts fl and rc, respectively.

The best-fitting model to the non-eclipse SIS and GIS data is shown in Fig. 3. The fit is not formally acceptable, with  $P_\nu(\chi_\nu^2) = 6.9 \times 10^{-3}$ . Most of the contributions to  $\chi^2$  come from the GIS data. This model fits the SIS data well, with  $P_\nu(\chi_\nu^2) = 0.34$ .

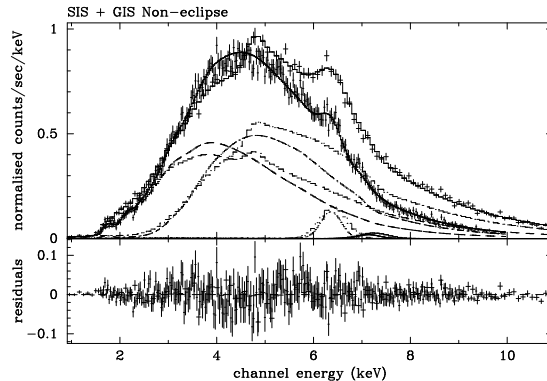


**Figure 3.** Non-eclipse SIS and GIS spectra fitted to the model of Equation 1.

### 3.2.2 Orbital dependence of the spectrum from the 1997 Observation

In order to follow the evolution of the spectrum through the eclipse, we divided the data into time intervals based on inspection of Fig. 1 and attempted to find a consistent model that could be used to parameterise the orbital dependence. The data were divided into the following five intervals: non-eclipse ( $\phi = -0.210 - -0.177$ ), pre-eclipse ( $\phi = -0.177 - -0.144$ ), ingress ( $\phi = -0.144 - -0.100$ ), early-eclipse ( $\phi = -0.100 - -0.044$ ), and mid-eclipse ( $\phi = -0.044 - +0.011$ ).

Fig. 4 shows the SIS spectra at different orbital phases. We see the iron line equivalent width increase as the eclipse ingress progresses and the continuum decays, while the spectrum becomes harder due to increased absorption. However, it is clear that there is a soft component which remains, even as the hard part of the spectrum continues to decrease. In Fig. 4 the 1994 mid-eclipse spectrum is also plotted. The soft component is clearly much weaker in this observation.

Table 1 shows the results of fits to a model of the form shown in Equation 1. In these fits we froze the interstellar column density  $N_H$  and the photon index of the direct beam from the pulsar  $\alpha$  at the pre-eclipse values. Otherwise, we were not able to extract meaningful confidence intervals from the fits to the early- and mid-eclipse phases as parameters became degenerate. As the eclipse progresses, the direct and Thomson-scattered emission components are replaced in the best-fitting model by the halo component. We thus conclude that the eclipse spectrum is dominated by the dust-scattered halo.

In order to investigate the orbital dependence of the iron line complex, we again split up the data but this time into 19 finer time intervals. The intervals were chosen to provide a compromise between counting statistics and time resolution. The exposures were typically 4–6 ks in the early parts of the observation, rising to 16 ks for the mid-eclipse phase. The lowest number of counts in any spectrum was 425. The spectra were rebinned so that each bin contained at least 30 counts. Each spectrum was fitted to a model which had an absorbed power law continuum and the fitting range was restricted to the 5–8 keV energy band. Because of the degeneracy between the line and continuum parameters, the

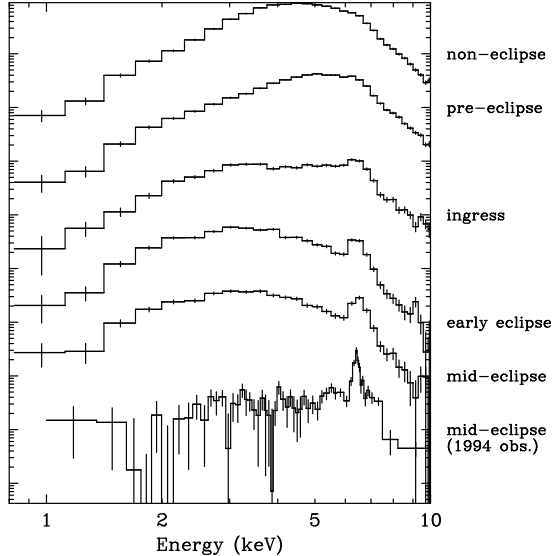


**Figure 4.** SIS0+1 spectra at different orbital phases. The orbital phases of the spectra correspond, from top to bottom, to those in Table 1. The mid-eclipse spectrum from the 1994 observation is also plotted at the bottom. For clarity, the intensity of each successive spectrum has been multiplied by a factor of 0.1.

absorption column density was fixed for the fits. The power law photon index was allowed to vary.

Fig. 5 shows the results of these fits when the iron line complex was modelled by a single Gaussian. When the line width was allowed to vary, both the line width and the line energy contained considerable scatter due to off-diagonal elements in the curvature matrix linking them. Thus, the line width was fixed at 0.25 keV (the observation-average value) for the fits. The line centroid energy increases from 6.45 keV in the pre-eclipse phase to 6.55 keV at mid-eclipse. The line intensity drops by an order of magnitude as the pulsar is eclipsed. To determine the time taken for this transition to occur, we fitted a simple continuous model to the intensity which assumes that the pre-eclipse and eclipse intensities are constant and that the intensity varies linearly during the ingress. We find that the transition occurs in  $20 \pm 9$  ks, corresponding to a projected distance of  $12 \pm 6$  lt-sec.

We fitted the iron-line region of the orbitally-resolved spectra with two narrow lines at 6.4 and 6.97 keV. As shown in Fig. 6, the two lines each undergo a partial eclipse. This means that the regions emitting these lines are larger than the companion star.

By looking at how long it takes for the individual iron lines to become eclipsed we can estimate the size of the emission regions for each of the ionic species (neutral and hydrogen-like iron). When we fit our simple intensity model to the line intensities in Fig. 6 we find that the line intensities decrease by factors of  $4.5 \pm 0.6$  and  $2.2 \pm 1.2$ , in intervals of  $30 \pm 19$  and  $> 23$  ks, for the 6.4 and 6.97 keV lines, respectively. These time intervals correspond to projected distances of  $19 \pm 12$ , and  $> 14$  lt-sec, respectively. Thus, the 6.4 keV line undergoes a deeper and more abrupt eclipse than the 6.97 keV lines. 80 per cent of the 6.4 keV emission is located within 19 lt-sec of the neutron star.

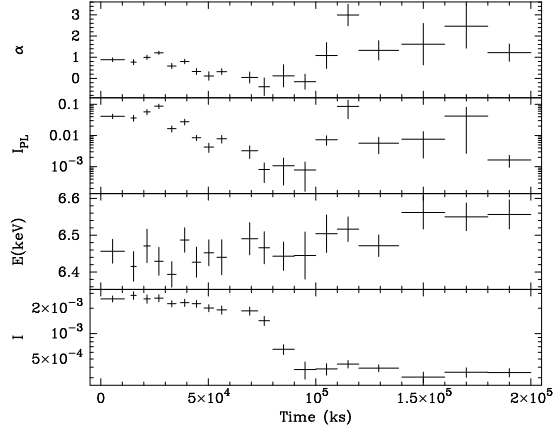


**Figure 5.** Orbital dependence of the iron line energy and intensity. The power law photon index is  $\alpha$ ,  $I_{PL}$  is the power law intensity in  $\text{cts s}^{-1} \text{cm}^{-2}$  at 1 keV,  $E$  is the Gaussian line centroid energy, and  $I$  is the line intensity in  $\text{cts cm}^{-2} \text{s}^{-1}$ .

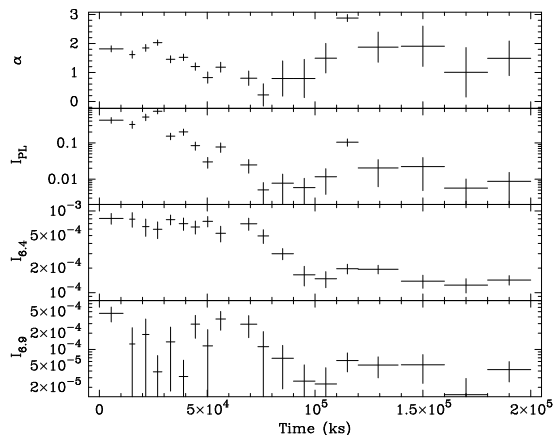


**Figure 6.** Orbital dependence of the iron line intensities for two narrow lines at 6.4 and 6.97 keV. The power law photon index is  $\alpha$ ,  $I_{PL}$  is the continuum power law intensity in  $\text{cts cm}^{-2} \text{s}^{-1} \text{keV}^{-1}$  at 1 keV, and the line intensities are in  $\text{cts cm}^{-2} \text{s}^{-1}$ .

### 3.2.3 The mid-eclipse spectrum

For this orbital phase we have data from both the 1997 and 1994 observations. We therefore discuss these together in this section. For the 1994 observation the intensity in the 2–10 keV band is  $6.5 \times 10^{-12} \text{ erg cm}^{-2} \text{ s}^{-1}$ . The iron line's equivalent width is 5.68 keV. The continuum is weak but a single power-law continuum is not acceptable. A model which gives an acceptable fit has a continuum composed of an absorbed power-law and a second power-law whose photon index is constrained to be equal to that of the first one plus 2 with less absorption, and two Gaussian emission lines whose centroid energy and width are free (see Fig. 7). Note that this model has a simpler continuum than the model described by Equation 1 and may be expressed as

$$I(E) = e^{-\sigma EN_{H1}} (I_h E^{-(\alpha+2)} + e^{-\sigma EN_{H1}} I_s E^{-\alpha} + \sum_{i=1}^N I_i e^{-(E-E_i)^2/2\sigma_i^2}) \quad (2)$$

**Table 1.** Best-fitting model parameters for fits to the orbital phase-resolved GIS and SIS data. The model is of the form shown in Equation 1. The interstellar absorption column and the photon index of the direct power law are fixed at the pre-eclipse values ( $N_{HI} = 7.61 \pm 0.35 \text{ cm}^{-2}$  and  $\alpha = 1.361 \pm 0.043$ ). Note how the direct and scattered continuum components ( $I_d$  and  $I_s$ ) are replaced by the dust-scattered halo component ( $I_h$ ) as the eclipse progresses.

Parameter	non-eclipse	pre-eclipse	ingress	early-eclipse	mid-eclipse
SIS Exposure (ks)	20.8	24.8	16.0	40.5	29.0
SIS count rate (cts $\text{s}^{-1}$ )	$3.30 \pm 0.01$	$1.62 \pm 0.01$	$0.451 \pm 0.005$	$0.205 \pm 0.002$	$0.142 \pm 0.002$
$I_d$ ( $10^{-3}$ cts $\text{cm}^{-2} \text{ s}^{-1}$ at 1 keV)	$33.5 \pm 2.2$	$8.8 \pm 1.4$	$2.90 \pm 0.61$	$0.39 \pm 0.35$	< 47
$N_{HI}$ $\text{cm}^{-2}$	$14.13 \pm 0.71$	$30.0 \pm 1.8$	$61.3 \pm 6.0$	$87 \pm 54$	$35 \pm 12$
$I_s$ ( $10^{-3}$ cts $\text{cm}^{-2} \text{ s}^{-1}$ at 1 keV)	$92.9 \pm 3.2$	$95.2 \pm 3.3$	$30.9 \pm 3.1$	$2.3 \pm 1.3$	$2.07 \pm 0.48$
$I_h$ ( $10^{-3}$ cts $\text{cm}^{-2} \text{ s}^{-1}$ at 1 keV)	< 13.1	$53.3 \pm 1.0$	$52.3 \pm 5.6$	$35.8 \pm 3.5$	$56.0 \pm 2.8$
$E_{\text{fit}}$ (keV)	$6.398 \pm 0.021$	$6.356 \pm 0.056$	$6.361 \pm 0.053$	$6.44 \pm 0.47$	$6.366 \pm 0.050$
$\sigma_{\text{fit}}$ (eV)	$195 \pm 54$	$227 \pm 88$	< 139	< 131	< 149
$I_{\text{fit}}$ ( $10^{-4}$ ctss $^{-1}$ )	$15.1 \pm 2.3$	$10.1 \pm 5.3$	$2.54 \pm 0.63$	$1.37 \pm 0.48$	$1.94 \pm 0.90$
$EW_{\text{fit}}$ (eV)					
$E_{\text{rc}}$ (keV)	$7.15 \pm 0.14$	$7.05 \pm 0.45$	$6.638 \pm 0.038$	$6.87 \pm 0.19$	$6.76 \pm 0.16$
$\sigma_{\text{rc}}$ (eV)	< 322	< 0.350	$214 \pm 135$	$233 \pm 116$	$207 \pm 77$
$I_{\text{rc}}$ ( $10^{-4}$ cts $\text{s}^{-1}$ )	$3.1 \pm 1.8$	< 8.95	$3.80 \pm 0.78$	$1.04 \pm 0.52$	$1.07 \pm 0.73$
$EW_{\text{rc}}$ (eV)					
$\chi^2_{\nu}$ /d.o.f	1.210/367	1.106/355	1.046/264	1.275/248	0.884/174
$P_{\nu}(\chi^2_{\nu})$	$3.52 \times 10^{-3}$	0.0826	0.292	$2.17 \times 10^{-3}$	0.862

for the case where there are  $N$  Gaussian emission lines. Here  $N_{Hi}$  is the interstellar column density and  $I_h$  is the intensity of the power law due to the dust halo.  $N_{HI}$  is the local column density for the absorbed power law, due to scattering of the direct pulsar emission in the stellar wind. The absorbed power law's intensity is  $I_s$ . The photon index of the absorbed, harder power law,  $\alpha$ , was fixed at 1.4 as it was found to be unconstrained by the data. The best-fitting parameters are shown in Table 2. The 1994 observation appears to have caught the source in a low-intensity state.

In contrast, the 1997 mid-eclipse spectrum has relatively strong continuum emission. The 2–10 keV flux is  $1.1 \times 10^{-11} \text{ erg cm}^{-2} \text{ s}^{-1}$ . Again, a model with two Gaussians was required to adequately fit the iron K-line region. The results are shown in Fig. 7 and Table 2.

### 3.3 Spatial analysis

From the slow decay of the soft-band lightcurves through the eclipse we suspected that an extended dust-scattered halo might be present. In order to investigate this we extracted SIS and GIS images in various energy bands. Surface brightness profiles were generated for the SIS and GIS data. The SIS was operated in one-CCD mode which is not optimal for studying structures extended over more than a few arcmin. This means that if we try to integrate a surface brightness profile over more than about 4 arcmin, we start including areas off the chip. Combined with the considerable azimuthal and energy dependence of the XRT, this complicates spatial analysis. Thus we used the ASCA-ANL software to generate ray-traced simulated images which we could compare with the data. In each case we simulated the image expected from a point source at the centroid coordinates of the observed source, and with the same spectrum. We then integrated the data to produce a radial surface brightness profile (SBP). We integrated the the ray-traced image in exactly the same way, from exactly the same region, to produce a SBP

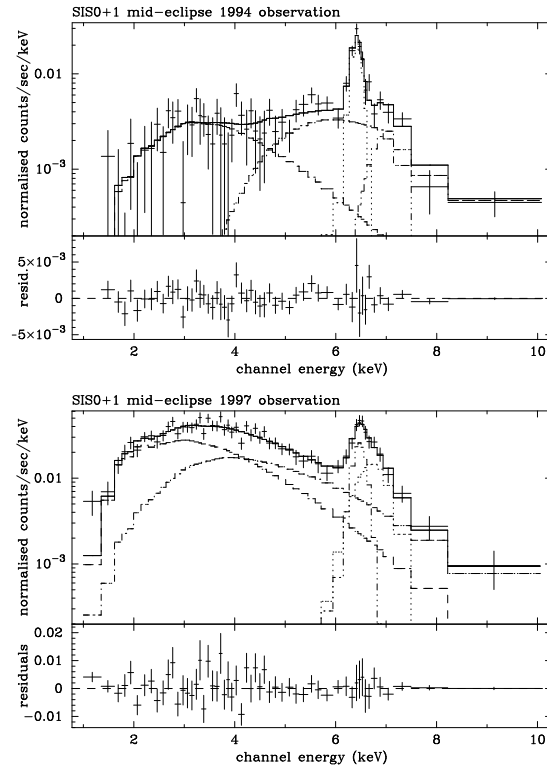


**Figure 7.** Top: SIS0+1 mid-eclipse spectrum and model for 1994 observation with fit residuals. Bottom: SIS0+1 mid-eclipse spectrum and model for 1997 observation with fit residuals. The data are for approximately the same orbital phases ( $-0.001$ – $+0.074$  for the 1994 observation and  $-0.044$ – $+0.011$  for the 1997 observation) and the same spectral binning has been applied. The model parameters are as shown in Table 2. Note the much stronger continuum in the 1997 observation.

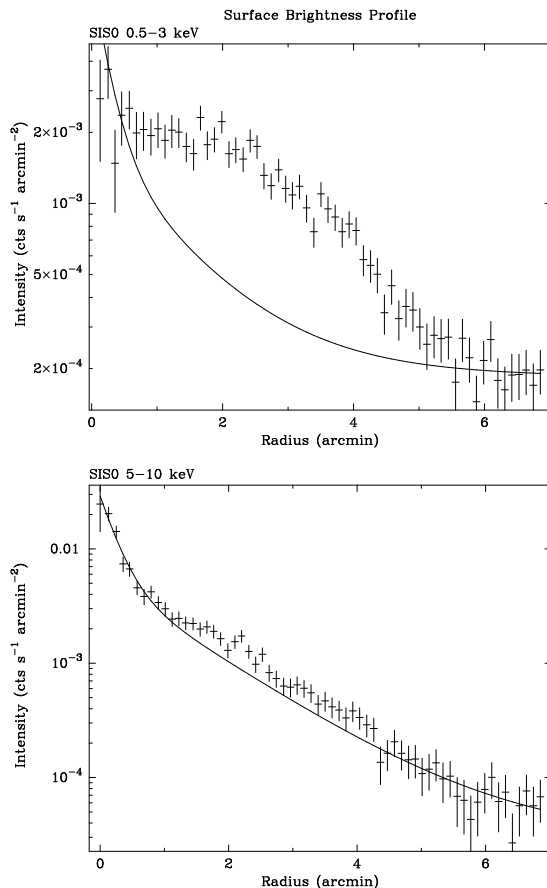
**Table 2.** Best-fitting model parameters for the mid-eclipse data of the 1994 and 1997 observations. The model is of the form shown in Equation 2 with two Gaussians representing iron fluorescence and recombination emission lines. The data are for approximately the same orbital phases ( $-0.001$ – $+0.074$  for the 1994 observation and  $-0.044$ – $+0.011$  for the 1997 observation) and the same spectral binning has been applied. Errors are for 90 per cent confidence in one interesting parameter.

Parameter		1994 Value	1997 Value
SIS Exposure	(ks)	29.0	40.9
SIS count rate	(cts s <sup>-1</sup> )	0.142 ± 0.002	0.026 ± 0.001
$N_{Hi}$	(10 <sup>22</sup> cm <sup>-2</sup> )	10.0 ± 2.6	6.67 ± 0.66
$I_h$	(cts cm <sup>-2</sup> s <sup>-1</sup> at 1 keV)	(6.1 ± 2.0) × 10 <sup>-3</sup>	0.028 ± 0.012
$N_{Hl}$	(10 <sup>22</sup> cm <sup>-2</sup> )	62 ± 16	< 6.20
$I_s$	(cts cm <sup>-2</sup> s <sup>-1</sup> at 1 keV)	(4.4 ± 1.5) × 10 <sup>-3</sup>	(1.57 ± 0.23) × 10 <sup>-3</sup>
$\alpha$		1.4 (fixed)	1.4 (fixed)
$E_{fl}$	(keV)	6.416 ± 0.018	6.474 ± 0.046
$\sigma_{fl}$	(eV)	41 ± 30	< 118
$I_{fl}$	(10 <sup>-4</sup> cts cm <sup>-2</sup> s <sup>-1</sup> )	1.54 ± 0.27	1.96 ± 0.96
$E_{rc}$	(keV)	7.13 ± 0.15	6.83 ± 0.17
$\sigma_{rc}$	(eV)	260 ± 190	< 380
$I_{rc}$	(10 <sup>-4</sup> cts cm <sup>-2</sup> s <sup>-1</sup> )	0.92 ± 0.39	2.3 ± 1.1
$\chi^2_{\nu}/\text{d.o.f}$		0.983/45	1.074/46

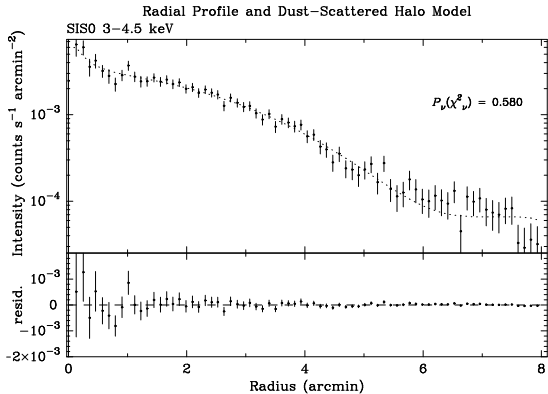
which represented the point spread function (PSF) expected from a point source at the same position with the same spectrum. We parameterised the PSF with three exponentials and fitted for the widths and relative normalizations. We then fitted the resulting three-exponential model, along with a constant background, to the SBP obtained from the data, keeping the widths and relative normalizations fixed. The fits were performed only for the innermost and outermost one arcmin of the SBP, where the point source and the background should dominate, respectively.

Fig. 8 shows surface brightness profiles from SIS0 for the 0.5–3 and 5–10 keV energy bands fitted to the PSF and a constant background. Comparing these, it is clear that the low-energy data require a spatially extended source, while the high-energy data are consistent with a point source and the XRT PSF. We interpret this as evidence for a dust-scattered halo.

We can obtain a rough measure of the halo intensity from the residuals of the fits but for a more quantitative analysis we decided to fit the SBPs to model haloes, convolved with the ray-traced PSF. We fitted the SBPs to a central point source, constant background, and dust-scattered halo. In the Rayleigh-Gans approximation the radial dependence of the model halo is  $[j_1(x)/x]^2$ , where  $j_1(x)$  is the spherical Bessel function of order 1 and  $x = (4\pi a/\lambda) \sin(\theta/2)$  (Hayakawa 1970). Here  $a$  is the grain radius,  $\lambda$  is the X-ray wavelength, and  $\theta$  is the angle through which the dust grain scatters the X-ray photon. The Rayleigh-Gans approximation is valid provided that  $4\pi a/\lambda \sin(\theta/2) \ll 1$ , which means in practice that we should restrict our analysis to energies above 1 keV (e.g. Smith & Dweck 1998). The observed angular distance of the detected X-ray photon from the centre of the image is  $\alpha = (1-z)\theta$ , where  $z$  is the distance from the observer to the dust grain divided by the distance from the observer to the source. The model was convolved with the ray-traced PSF for the fit. To simplify computation, instead of using the Bessel-function form above we used the Gaussian approximation of Mauche & Gorenstein (1986) for the halo shape. Figure 9 shows typical fit results for an SIS0 eclipse



**Figure 8.** SIS0 surface brightness profile for the mid-eclipse phase of the 1997 observation. The data are fitted to the XRT PSF plus a constant for radii less than 1 arcmin and between 6 and 7 arcmin. Top: 0.5–3 keV. Bottom: 5–10 keV.



**Figure 9.** 3.0–4.5 keV surface brightness profile for OAO 1657–415 for the mid-eclipse phase of the 1997 observation. The data have been fitted to a central point source, constant background, and dust-scattered halo.

halo. We divided the SIS0 and SIS1 eclipse data into energy bins (1.5–2.5, 2.5–3.5, 3.5–4.5, 4.5–5.5, and 5.5–7.0 keV) and obtained the best-fitting value of  $4\pi a/\lambda$  for each energy bin, assuming that the dust grains were distributed uniformly along the line of sight. We then plotted  $4\pi a/\lambda$  against energy and the slope yielded the value  $0.095 \pm 0.005 \mu\text{m}$  for the size of the dust grains.

The size distribution of the grains may be found either from the time dependence of the integrated halo spectrum (Xu et al. 1986) or from the surface brightness profile at a given energy (Mauche & Gorenstein 1986). Since we find it easier to separate the central source from the halo in discrete energy bands by deconvolving the surface brightness profile from the point spread function, we adopt the latter approach. We do not have good enough counting statistics for the former method.

We split the SIS0 and SIS1 eclipse data into 20 ks (gross) bins and extracted surface brightness profiles for different energy ranges (1.5–2.5, 2.5–3.5, 3.5–4.5, 4.5–5.5, and 5.5–7.0 keV). We obtained the halo intensity for each time and energy bin. We then fitted these halo intensities with an exponential function for each energy bin. The spatial resolution of the GIS is such that the profiles are more smeared out. This means that the GIS values for the decay time constant have larger error bars and in some cases are not constrained by the data. Thus, although the GIS results for the decay time constant are consistent with the SIS results, we use only the SIS data to obtain the decay time constant. If we assume the dust is uniformly distributed along the line of sight, we expect the halo to decay exponentially with a time constant of  $t_d(E) = 13.6E^{-2}D_8a_{0.1}^2$  d, where  $E$  is the photon energy in keV,  $D_8$  is the distance to the source in units of 8 kpc, and  $a_{0.1}$  is the dust grain radius in units of  $0.1 \mu\text{m}$ . A fit of this form to the data is shown in Fig. 10. This results in a distance of  $(7.9 \pm 0.9)a_{0.1}^2$  kpc for OAO 1657–415. We have implicitly assumed here that the eclipse is a step-function. The eclipse ingress is much shorter than the eclipse duration and, as our measurements of the source intensity start just before eclipse ingress, it seems reasonable to assume a constant intensity prior to the eclipse ingress. However, this estimate of the distance is sensitive to the distribution of the dust along the line of sight. If the dust is all in a sheet

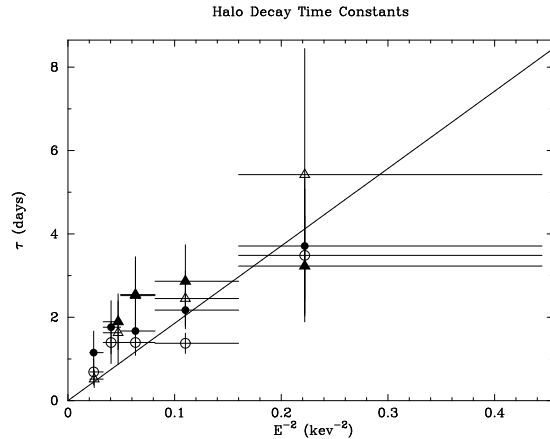


**Figure 10.** Halo decay time-constants plotted against the inverse square of the energy. The SIS0, SIS1, GIS2, and GIS3 data are represented by open circles, filled circles, open triangles, and filled triangles, respectively. The data have been fitted to a function of the form  $t_d(E) = \tau E^{-2}$  and the best-fitting value is  $\tau = 18.6 \pm 2.3$  d.

half-way to the source our estimate for the distance becomes  $(12.7 \pm 1.5)a_{0.1}^2$  kpc, while it is  $(4.56 \pm 0.54)a_{0.1}^2$  kpc if the sheet is at either 10 or 90 per cent of the distance to the source.

## 4 DISCUSSION

### 4.1 Intensity States

We have observed OAO 1657–415 during the latter half of its eclipse in two distinct intensity states and have found differences in the spectra. The low-state spectrum is consistent with an absorbed power law with photon index  $0.36 \pm 0.19$  due to scattered and absorbed emission from the pulsar, combined with a dust-scattered halo and fluorescent emission from cold iron. The high-state spectrum has a stronger continuum which is due to scattering of the direct pulsar emission in the stellar wind combined with the dust-scattered halo. In the high state the recombination line due to ionised iron is stronger than the fluorescent line. In the low state the fluorescent line is stronger. This difference between the two states is most likely due to increased photoionization of the stellar wind in the high-intensity state.

### 4.2 The spectra

The aim of the 1997 observation was to use the eclipse of OAO 1657–415 to study the outer atmosphere of the OB companion star and its vicinity by mapping out the X-ray emission in the system. As the eclipse ingress progresses, the X-ray emission must propagate through the wind and outer atmosphere of the OB star. From the progress of the partial eclipses of the iron emission lines we conclude that the 6.4-keV fluorescent emission originates near the neutron star while the 6.9-keV recombination emission comes from the extended wind of the companion.

We find that a single power law cannot describe the continuum spectrum outside of eclipse. We obtained an accept-

able fit using two power laws with the same photon index, one of which has a larger absorption column density than the other. This model is equivalent to a partially-covered power law. Similar two-component continua have been observed in Cen X-3 (Ebisawa et al. 1996; Audley 1997), Vela X-1 (Sako et al. 1999), and GX1+4 (Endo 2001). Sako et al. (1999) claim that the more absorbed component is the direct beam which is absorbed by the stellar wind surrounding the neutron star and that the less-absorbed component is due to scattering in the stellar wind. Ebisawa et al. (1996) claim the opposite: that the direct beam is the less-absorbed component. One way to distinguish between these two pictures is by pulse-phase-resolved spectroscopy of the continuum. We would expect the component that is due to the direct beam to pulsate at the pulsar frequency. As long as the light travel time over the extent of the stellar wind is at least a significant fraction of the pulse period, pulsations in the scattered component should be smeared out. Endo (2001) did this in the case of GX1+4 and found that both components originate near the neutron star. Audley (1997) came to the same conclusion for Cen X-3. When we fit the pulse-phase resolved non-eclipse SIS data with the two-power law model, we find that the intensities of the power laws have essentially the same dependence. We therefore conclude that both of these components must originate at the same place, significantly less than 38 lt-sec away from the neutron star.

### 4.3 The dust-scattered halo

Scattering of X-rays by interstellar dust leads to the formation of a halo whose intensity, shape, and spectral properties depend on the distance to the source, its intrinsic spectrum, the distribution of dust grains, and their size and composition (Hayakawa 1970). Trümper & Schönfelder (1973) proposed that the time-dependence of a dust-scattered halo from a variable X-ray source could be used to determine the distance to the source and the distribution of dust along the line of sight. Xu et al. (1986) suggested that high-mass X-ray binaries with their abrupt total eclipses that occupy a large fraction of the orbit would be good candidates for this kind of study. Mitsuda et al. (1990) used lunar occultation observations with Ginga of two X-ray sources to study the energy dependence of the dust halo and inferred the presence of iron in the scattering grains. Day & Tennant (1991) applied the model of Molnar & Mauche (1986) for the X-ray halo of a time-varying source to the low-energy eclipse lightcurve of Cen X-3 and obtained a distance of 5 kpc and a dust grain radius of  $0.33 \mu\text{m}$ . Woo et al. (1994) used the imaging capability of ASCA's SIS to measure the surface brightness profile of the dust-scattered halo in Cen X-3 and infer some properties of the dust grains. Applying the Rayleigh-Gans approximation, from the lower than expected relative intensity of the halo they concluded that the dust grains were loose aggregates rather than solid particles. However, Smith & Dweck (1998) later pointed out that the Rayleigh-Gans approximation for the differential scattering cross-section overestimates the halo intensity below 1 keV and that when the more exact Mie solution is used the data may be consistent with solid grains. Later, Draine (2003) pointed out that the median scattering angle for the dust halo would be small enough that most of the halo photons would be seen in the core of the ASCA

image which is dominated by the central point source. This would have led Woo et al. (1994) to underestimate the halo intensity and is likely to be a problem with the current observation of OAO 1657–415. Predehl et al. (2000) demonstrated that Chandra could be used to determine the distance to Cyg X-3 to within 20 per cent by correlating the lightcurves at different radii from the source. Cyg X-3 only undergoes a partial eclipse while high mass X-ray binaries such as OAO 1657–415 undergo total eclipses for large fractions of their orbital periods. This makes a high-mass X-ray binary such as OAO 1657–415 a promising candidate for this kind of study.

We have found a decaying dust-scattered halo in the eclipse of OAO 1657–415 (see Figure 1). The half-power radius of the halo is about 4 arcmin, which is not much larger than the XRT point spread function that smears out the halo and mixes in flux from the core (see Figure 9). The X-ray spectrum of OAO 1657–415 in eclipse has three components: the dust halo, X-rays from the eclipsed pulsar scattered by the primary's atmosphere, and emission (mostly iron-line recombination) from the primary's atmosphere. Only the dust halo will appear to be extended in an X-ray image. Because this source is heavily absorbed ( $N_H \sim 5 \times 10^{22} \text{ cm}^{-2}$ ) the halo is mostly seen above the ROSAT pass-band.

Chakrabarty et al. (1993) used the observed values of the pulse period and its derivative during a steady spin-up interval to place a lower limit of  $\sim 11$  kpc on the distance to OAO 1657–415. Chakrabarty et al. (2002) found a distance of  $6.4 \pm 1.5$  kpc from the reddening of the optical counterpart. The distance we estimated from the decay of the halo,  $(7.9 \pm 0.9)a_{0.1}^2$  kpc, lies between these two values. It is interesting to compare the case of Cen X-3 where Day & Tennant (1991) obtained a distance of  $5.4 \pm 0.3$  kpc which is a little lower than the lower limit derived from the relation between temperature and luminosity for the BO star (6.2 kpc; Krzemiński 1974). The value we obtained for the maximum dust-grain radius is  $0.095 \pm 0.005 \mu\text{m}$  which is smaller than the value obtained by Day & Tennant (1991) ( $0.34 \pm 0.01 \mu\text{m}$ ). There may be systematic effects resulting from our simplistic assumptions which causes us to underestimate the distance and overestimate the grain size. We would like to point out, however, that the distance and grain size estimates are independent; the measured halo intensity does not depend on the assumed grain distribution. Our estimate of the distance is sensitive to the exact distribution of the dust along the line of sight; we have assumed that it is uniformly distributed. Our results also depend on the assumption that the intrinsic intensity and spectrum of the source were constant before eclipse.

## 5 CONCLUSIONS

The eclipse spectrum of the source in its high-intensity state is dominated by the decaying dust-scattered halo. We estimate the radius of the grains to be  $0.095 \pm 0.005 \mu\text{m}$  and the distance to the source to be  $(7.9 \pm 0.9)a_{0.1}^2$  kpc, where  $a_{0.1}$  is the grain radius in units of  $0.1 \mu\text{m}$ . Using our estimate for the grain size, the distance to the source becomes  $7.1 \pm 1.3$  kpc. We find that the non-eclipse high-state continuum spectrum cannot be modeled by a single power law. A more-absorbed component due to scattering by material



near the pulsar is required. The iron lines underwent partial eclipses during the 1997 observation. We estimate that 80 per cent of the 6.4-keV fluorescent emission originated less than  $19 \pm 12$  lt-sec away from the pulsar while the 6.9-keV recombination line was mostly emitted by the extended, ionised stellar wind. During the 1994 observation, the continuum emission was much lower and the iron emission during eclipse was dominated by the 6.4-keV fluorescent line, which suggests that the source was in a low intensity state.

#### ACKNOWLEDGMENTS

MDA was supported by a fellowship from the Japan Society for the Promotion of Science. This research has made use of data obtained through the High Energy Astrophysics Science Archive Research Center Online Service, provided by the NASA/Goddard Space Flight Center. We would like to thank Naomi Ota and Ryo Shibata for help with the ray-tracing software. We are grateful to the referee, Peter Predehl, for his helpful comments.

#### REFERENCES

- Audley M. D., 1997, PhD thesis, University of Maryland  
 Baykal A., 1997, *A&A*, 319, 515  
 Baykal A., 2000, *MNRAS*, 313, 637  
 Bildsten L., Chakrabarty D., Chiu J., Finger M. H., Koh D. T., Nelson R. W., Prince T. A., Rubin B. C., Scott D. M., Stollberg M., Vaughan B. A., Wilson C. A., Wilson R. B., 1997, *ApJS*, 113, 367  
 Chakrabarty D., Grunsfeld J. M., Prince T. A., Bildsten L., Finger M. H., Wilson R. B., Fishman G. J., Meegan C. A., Paciesas W. S., 1993, *ApJ*, 403, L33  
 Chakrabarty D., Wang Z., Juett A. M., Lee J. C., Roche P., 2002, *ApJ*, 573, 789  
 Choi C. S., Dotani T., Day C. S. R., Nagase F., 1996, *ApJ*, 471, 447  
 Corbet R. H. D., 1986, *MNRAS*, 220, 1047  
 Day C. S. R., Tennant A. F., 1991, *MNRAS*, 251, 76  
 Dotani T., Kii T., Nagase F., Makishima K., Ohashi T., Sakao T., Koyama K., Tuohy I. R., 1989, *PASJ*, 41, 427  
 Draine B. T., 2003, *ApJ*, 598, 1026  
 Ebisawa K., Day C. S. R., Kallman T. R., Nagase F., Kotani T., Kawashima K., Kitamoto S., Woo J., 1996, *PASJ*, 48, 425  
 Endo T., 2001, PhD thesis, Tokyo University  
 Hayakawa S., 1970, *Prog. Theor. Phys.*, 43, 1224  
 Kamata Y., Koyama K., Tawara Y., Makishima K., Ohashi T., Kawai N., Hatsukade I., 1990, *PASJ*, 42, 785  
 Koyama K., Awaki H., Kunieda H., Takano S., Tawara Y., Yamamuchi S., Hatsukade I., Nagase F., 1989, *Nature*, 339, 603  
 Krzemiński W., 1974, *ApJ*, 192, L135  
 Levine A., Rappaport S., Putney A., Corbet R., Nagase F., 1991, *ApJ*, 381, 101  
 Mauche C. W., Gorenstein P., 1986, *ApJ*, 302, 371  
 Mitsuda K., Takeshima T., Kii T., Kawai N., 1990, *ApJ*, 353, 480  
 Molnar L. A., Mauche C. W., 1986, *ApJ*, 310, 343  
 Polidan R. S., Pollard G. S. G., Sanford P. W., Locke M. C., 1978, *Nature*, 275, 296+  
 Predehl P., Burwitz V., Trümper J., 2000, *A&A*, 357, L25  
 Sako M., Liedahl D. A., Kahn S. M., Paerels F., 1999, *ApJ*, 525, 921  
 Smith R. K., Dweck E., 1998, *ApJ*, 503, 831  
 Trümper J., Schönfelder V., 1973, *A&A*, 25, 445  
 White N. E., Pravdo S. H., 1979, *ApJ*, 233, L121  
 Woo J. W., Clark G. W., Day C. S. R., Nagase F., Takeshima T., 1994, *ApJ*, 436, L5  
 Xu Y., McCray R., Kelley R., 1986, *Nature*, 319, 652